

Star formation in the Vela Molecular Clouds: A new protostar powering a bipolar jet[★]

T. Giannini¹, F. Massi², L. Podio^{2,3}, D. Lorenzetti¹, B. Nisini¹,
A. Caratti o Garatti^{1,4}, R. Liseau⁵, G. Lo Curto⁶, and F. Vitali¹

¹ INAF - Osservatorio Astronomico di Roma, via Frascati 33, 00040 Monteporzio Catone, Italy
e-mail: [giannini;caratti;lorenzetti;nisini;vitali]@mporzio.astro.it

² INAF - Osservatorio Astrofisico di Arcetri, Largo E. Fermi 5, 50125 Firenze, Italy
e-mail: [fmassi;lindapod]@arcetri.astro.it

³ Università degli Studi di Firenze, Piazza S.Marco 4, 50121 Firenze, Italy

⁴ Università degli Studi di Roma “Tor Vergata”, via della Ricerca Scientifica 1, 00133 Roma, Italy

⁵ Stockholm Observatory, AlbaNova University Centre, 10691 Stockholm, Sweden
e-mail: rene@astro.su.se

⁶ European Southern Observatory, Casilla 19001, Santiago 19, Chile
e-mail: gloturto@eso.org

Received 6 September 2004 / Accepted 24 November 2004

Abstract. We have performed a detailed study of the star-forming region associated with the IRAS source 08448-4343 in the cloud D of the Vela Molecular Ridge. Our investigation covers a wide spectral range from the near IR, through the thermal IR to the mm-band exploiting both imaging and spectroscopic facilities in each spectral regime. A picture emerges of a dust structure which hosts a near IR cluster and multiple well-collimated H₂ jets; these jets originate from different sources lying in a compact region at the cluster centre. The peak of the 1.2 mm map does not coincide with the IRAS peak, thus tracing a less evolved and denser region with a colder dust with respect to that traced by IRAS. This view is also confirmed by the observations of CS transitions from $J = 2-1$ to $J = 7-6$. The mm peak can be associated with the position of a red object, already proposed in previous studies as the driving source of the main jet in the field. This jet, extended along more than 0.3 pc, is composed of individual knots whose radial velocities decrease with increasing distance from the central source, which is resolved into at least six 2 μ m peaks. The reddest and coldest of these peaks is well aligned with the inner knots of the jet. The spectral energy distribution of the central source resembles that of an intermediate luminosity, Class I protostar, whose youth is discussed in terms of the efficiency of the energy transfer into the jet.

Key words. stars: circumstellar matter – stars: individual: IRAS08448-4343 – ISM: jets and outflows – infrared: ISM – ISM: lines and bands – radio continuum: ISM

1. Introduction

The modalities of the interplay between the activity occurring inside a molecular cloud and the star formation process which takes place in its interior have a major role in determining the evolution of the galaxies. However, current facilities operating at infrared (IR) and millimetre (mm) wavelengths allow us to penetrate, with the adequate scale and sensitivity, only relatively few clouds of our Galaxy. If one plans to apply the derived properties to external (spiral) galaxies, particular care has to be exerted in selecting molecular clouds that are as much as possible representative of what we expect to sample in those galaxies, i.e. essentially their disks. This motivated an observational study we have undertaken for some years

(Liseau et al. 1992; Massi et al. 1999 (hereafter M99), 2000; Lorenzetti et al. 1993, 2002, (hereafter L02); Massi et al. 2003; Caratti o Garatti et al. 2004), aimed to characterize star formation regions located in the galactic plane, emphasizing both their dynamical properties and the interactions with the surrounding molecular cloud. The present paper refers to the region IRAS08448-4343, listed as IRS17 according to our internal classification (Liseau et al. 1992). This region is located at about 700 pc from the Sun, within one out of the four giant clouds which constitute the Vela Molecular Ridge (VMR), the one named the D-cloud by Murphy & May (1991). Through near IR imaging we have investigated the young stellar content of the D-region, and found evidence for clustering in the IRS17 field (M99, Massi et al. 2000, 2003). A preliminary insight into the kinematical and physical properties of IRS17, through narrow band and near IR spectroscopy, has shown a

[★] Based on observations collected at the European Southern Observatory, Chile (66.C-158, 68.C-0020, 69.C-0175, 71.C-0088).

Table 1. Journal of observations.

Imaging							
Telescope/Instrument	Date	Filter		t (s)			
VLT/ISAAC-SW	6 Feb. 2001	[FeII]1.64, H ₂ 2.12, Bry		480			
		K_s, H		60			
VLT/ISAAC-LW		L, M		600			
3.6 m/TIMM12	25-26 Mar. 2004	N10.4		3000			
SEST/SIMBA	23 May 2003	1.2 mm		5670 ^a			
Infrared Spectroscopy							
Telescope/Instrument	Date	$\lambda/\Delta\lambda$	PA (°)	Covered Knots	t (s)		
NTT/SofI HK grism	13 Mar. 2003	600	153	D,F	2400		
VLT/ISAAC-SW 2.12 μm	5 Feb. 2001	8900	153	D,F	1800		
			150.5	C,G			
			161	A,B,C			
			131.5	E,F			
			137	A			
Millimetre Spectroscopy							
SEST Receiver	Date	Line	ν (GHz)	θ_{HPBW} ($''$)	N^b	$\Delta\nu$ (km s ⁻¹)	t (s)
IRAM115	4-8 Jun. 1994	CS(2-1)	97.98	57	43	0.132	6060
IRAM230		CS(5-4)	244.94	23	28	0.053	4980
NDW350		CS(7-6)	342.88	15	12	0.038	8400
IRAM115		C ³⁴ S(2-1)	96.41	57	18	0.134	16200

Note: ^a Time spent to integrate over an area of $18' \times 14'$ in fast scanning mode.

^b Number of the map points.

protostellar jet characterized by H₂ line emission and propagating into the dense and obscured neighbourhood (L02). Such a jet emanates from a source near the centre of the cluster, but different from the object identified as the near-infrared counterpart of the IRAS source, which is the most luminous object in the field. This has been spectroscopically observed recently in the 3–5 μm range by Dartois et al. (2003): from the strong 3 μm absorption feature of ice water present in the spectrum, a measure of the visual extinction of ~ 20 mag can be estimated toward the IRAS source. Large-scale studies of the IRS17 region have been conducted few years ago in the mm wavelengths. Wouterloot & Brand (1999, hereafter WB99) have mapped nine sources in VMR, including IRS17 (their WB89 1181), in ¹²CO(1–0), ¹³CO(1–0), C¹⁸O(1–0) and CS(2–1) transitions, revealing the presence of a molecular clump, but leaving open the question of the existence of a CO outflow. Quite recently, Faundez et al. (2004) included IRS17 in their SIMBA survey of southern high-mass star-forming regions, deriving the physical characteristics of the molecular core.

To obtain a deeper view into the IRS17 structure, we have carried out a multifrequency study of the field. Our aims are to: i) clearly identify the source powering the jet and its evolutionary stage; ii) derive the dynamical properties of the jet; iii) define the physical parameters of the molecular cloud harboring the protostellar cluster. Our observations are presented in Sect. 2. We have imaged the field in the near and thermal IR (at higher spatial resolution than the previous observations) and completed by means of medium-resolution observations

($R \sim 9000$) the spectroscopic study of the jet presented by L02. The molecular cloud core was studied through millimetre observations in the continuum and in selected CS lines. In Sect. 3 we analyze the data and discuss our results; Sect. 4 summarizes our conclusions.

2. Observations and results

The observations presented in this paper were collected using ESO facilities from 1994 to 2004. They are summarized in Table 1.

2.1. Infrared observations

2.1.1. Imaging

Broadband H , K_s , L , M and narrowband images in the [Fe II] ($\lambda = 1.64 \mu\text{m}$, $\Delta\lambda = 0.025 \mu\text{m}$), H₂ 1–0S(1) ($\lambda = 2.13 \mu\text{m}$, $\Delta\lambda = 0.028 \mu\text{m}$) and Bry ($\lambda = 2.17 \mu\text{m}$, $\Delta\lambda = 0.028 \mu\text{m}$) filters were obtained in February 2001 with the ISAAC camera (Cuby et al. 2004) at the Very Large Telescope (VLT, Paranal, Chile). Imaging in the N10.4 broadband filter was carried out in March 2004 with TIMM12 (Doublier et al. 2003) at the 3.6 m ESO telescope (La Silla, Chile). The field of view of the short wavelength images is $2.5' \times 2.5'$ (scale of 0.1484 arcsec/px), while in the L and M filters the sky area covered is $72'' \times 72''$ (scale of 0.071 arcsec/px). In the N band we adopted a scale of 0.3 arcsec/px, corresponding to a field of view of $96'' \times 72''$. All the images are centred on the IRAS peak ($\alpha_{2000} = 08^{\text{h}}46^{\text{m}}34.8^{\text{s}}$,

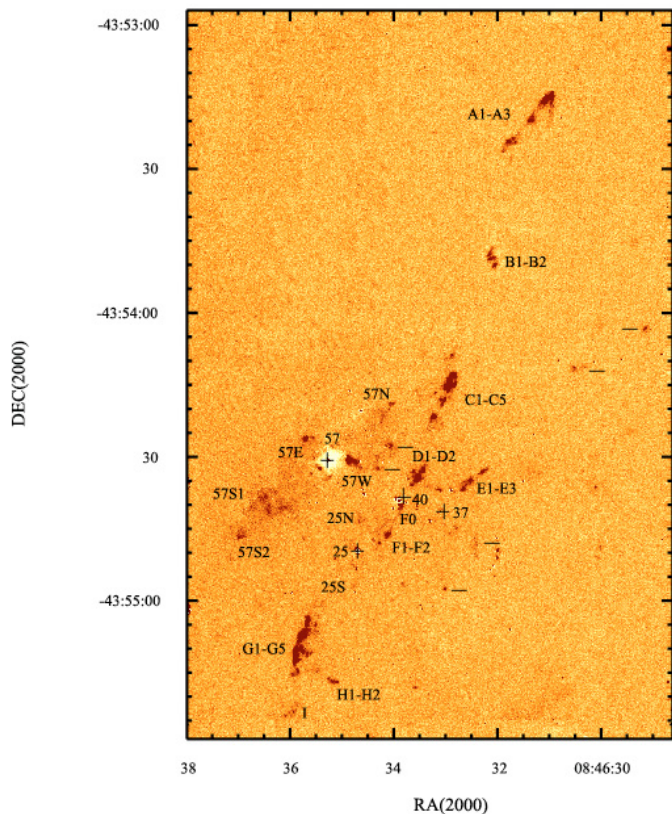


Fig. 1. H_2 continuum subtracted image. In the field at least five jets are recognizable: a main jet more than 0.3 parsec long, composed by the knots from A to I and four other jets composed by the knots E1–E3, 57N–S, 57E–W and 25N–S, respectively. Other H_2 condensations not clearly associated with any of the cited jets are indicated with a dash. The positions of the candidate exciting sources (# 25, 37, 40, 57 in our internal classification, M99) are indicated with a cross. Source #57 is the near-infrared counterpart of IRAS08448-4343.

$\delta_{2000} = -43^\circ 54' 31''$). The observations were obtained by nodding and jittering the telescope around the pointed position in the usual ABB'A' mode. In L , M and N bands chopping was also performed.

The raw data were reduced by using standard procedures for bad pixel removal, flat fielding and sky subtraction. Continuum-free images in the narrowband filters were obtained as a first step by subtracting appropriately scaled K_s and H images from the H_2 , Bry and $[Fe II]$ images. Such scaling has been obtained by performing the photometry of a number of stars located in different positions within the field. Out of the three continuum-subtracted narrowband images, only that in the H_2 2.12 μm filter shows a signal above the 3σ limit ($9 \times 10^{-17} \text{ erg s}^{-1} \text{ cm}^{-2} \text{ arcsec}^{-1}$), while no emission is recognizable down to 1σ both in the $[Fe II]$ and Bry images. Given the closeness of the effective wavelength of the H_2 and Bry filters, we have thus decided to use the Bry image for the continuum subtraction from the H_2 image. The H_2 , continuum-free image was flux calibrated by adopting the H_2 photometry by L02 and is shown in Fig. 1. Together with a sub-parsec scale jet already known from our previous studies, other mass flow

manifestations are clearly recognizable in the field; we will comment on them in Sect. 3.1.

H and K_s images were flux calibrated on the basis of the previous observations by M99, while a photometric standard star (HD75223) was observed to calibrate the images in L and M filters. Finally, since the calibration of the N image suffers from the absence of a photometric standard star, the image was calibrated by assigning to the source #57 (identified as the near-infrared counterpart of the IRAS source, M99) the flux measured by IRAS at 12 μm , which amounts to 8.7 Jy. The IRAS filter is broader than the TIMMI2 N10.4 filter, and has a different spectral response. To check the accuracy of our procedure, we have compared the $N10.4$ magnitudes of a sample of TIMMI2 standard stars with their 12 μm IRAS flux, finding discrepancies which never exceed ~ 0.2 mag. Such a conservative estimate has been counted as an additional contribution to the N photometric uncertainty (see Table 4). The portions of the L , M , and N images where emission above the 3σ level (limiting magnitudes: $L \sim 15.8$, $M \sim 12.8$, $N \sim 7$) has been detected are shown in Fig. 2. The H and K_s images are morphologically similar to those obtained with the IRAC2 camera (Moorwood et al. 1992) by M99 (their Fig. 2), so they are not shown here. Absolute α and δ positions were derived by the astrometry of M99 (their Table 4), which provides an accuracy of about 1 arcsec both in RA and Dec. Astrometry in L , M and N bands has been obtained by assigning to the stars in the field the same coordinates as their counterparts in the K_s frame, having assumed that the brightest object in each image corresponds to source #57. Given the plate scale of the L , M and N images the accuracy of ~ 1 arcsec is preserved.

2.1.2. Low-resolution spectroscopy

The 1.55–2.50 μm , low-resolution spectra of most of the knots associated with the main jet in the IRS17 field have been reported in L02. In March 2003 we used the SofI spectrometer (Lidman et al. 2003) at the New Technology Telescope (NTT, La Silla, Chile) to target the two knots (namely D and F) closest to the candidate exciting source (#40, L02), which remained unobserved during our previous observations. Long slit spectroscopy in the 1.55–2.50 μm range was carried out in the ABB'A' mode with the $1'' \times 290''$ slit ($R \sim 600$), with a total integration time of 2400 s. The observations were flat-fielded, sky subtracted and corrected for the optical distortions along both the spatial and spectral directions. Telluric features were removed by ratioing the extracted spectra by that of a blackbody-normalized telluric standard star, once corrected for its intrinsic spectral features. Wavelength calibration was derived from the lines of a xenon-argon lamp. Flux calibration was obtained by adopting the narrowband photometry in the H_2 2.12 μm line provided by L02, which is given with an uncertainty within 20%.

In Table 2 the identified lines along with the measured fluxes are given. The associated uncertainty refers to the rms of the local baseline. The line spectra are substantially similar to those exhibited by the outer knots (L02), the bulk of the emission being in the form of H_2 rovibrational lines from

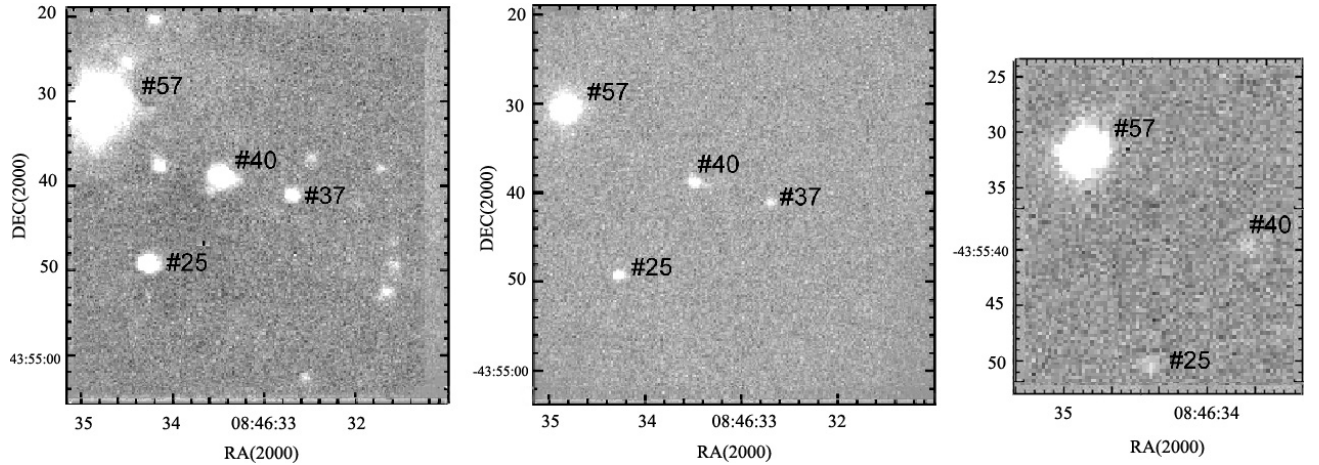


Fig. 2. Portions of the *L* (left), *M* (middle) and *N* (right) images of the IRS17 field. Sources exciting the jets are labelled.

Table 2. Line emission fluxes for the knots D and F.

λ (μm)	Ident.	D1	F1	IRS 40+F0
		$F \pm \Delta F$ (10^{-15} erg s $^{-1}$ cm $^{-2}$)		
1.644	[FeII]a 4 D $_{7/2}$ -a 4 F $_{9/2}$			0.8 ± 0.3^a
1.686	(1, 0)S9	0.7 ± 0.2	–	–
1.714	(1, 0)S8	0.5 ± 0.2^a	–	–
1.748	(1, 0)S7	1.5 ± 0.1	0.3 ± 0.1	0.4 ± 0.1
1.788	(1, 0)S6	1.4 ± 0.1	0.6 ± 0.1	–
1.958	(1, 0)S3	38.1 ± 0.6	4.2 ± 0.4	5.4 ± 0.2
2.004	(2, 1)S4	1.4 ± 0.1	–	–
2.034	(1, 0)S2	8.2 ± 0.2	2.0 ± 0.3	–
2.073	(2, 1)S3	1.8 ± 0.2	0.9 ± 0.3	–
2.122	(1, 0)S1	27.8 ± 0.2	7.9 ± 0.1	6.1 ± 0.2
2.154	(2, 1)S2	1.1 ± 0.1	–	–
2.224	(1, 0)S0	9.4 ± 0.4	2.1 ± 0.2	1.7 ± 0.4
2.247	(2, 1)S1	3.5 ± 0.4	1.1 ± 0.2	1.0 ± 0.2
2.407	(1, 0)Q1	54.2 ± 0.4	11.8 ± 0.2	8.2 ± 0.4
2.414	(1, 0)Q2	20.3 ± 0.5	3.9 ± 0.2	4.1 ± 0.4
2.424	(1, 0)Q3	48.7 ± 0.5	10.6 ± 0.2	6.6 ± 0.4
2.438	(1, 0)Q4	21.4 ± 0.5	6.6 ± 0.2	4.5 ± 0.5
2.455	(1, 0)Q5	11.2 ± 0.5	12.9 ± 0.2	6.5 ± 0.4
2.476	(1, 0)Q6	16.3 ± 0.6	–	1.8 ± 0.4
2.501	(1, 0)Q7	29.0 ± 0.6	–	–

Note: a Signal-to-noise ratio less than three

low-lying energetic levels (excitation energy up to ~ 16000 K). However, a faint [FeII] $1.64 \mu\text{m}$ line is present in the spectrum of source #40 (which is also contributed by the emission of the faint knot denoted as F0 in Fig. 1) at about a 2.7σ level, possibly suggesting that higher excitation conditions exist at the jet basis. Following the analysis of the H $_2$ rotational diagrams as described by L02, we have simultaneously derived the visual extinction and the temperature, which are $A_V = 30 \pm 3$ mag and $T = 2200 \pm 160$ K in all the targeted positions. We will discuss these results in the next section.

2.1.3. Medium-resolution spectroscopy

Medium-resolution spectra of the H $_2$ $2.1218 \mu\text{m}$ line along the main jet were obtained in February 2001 with ISAAC. We used the $0.3'' \times 120''$ slit, which corresponds to a nominal resolution

of about 8900 , i.e. 33.7 km s^{-1} . The covered knots along with the slit position angle and the total integration time are indicated in Table 1. We adopted the same acquisition/reduction techniques as outlined in the previous section. Wavelength calibration was done using OH atmospheric lines (Rousselot et al. 2000), which provide an accuracy within 3 km s^{-1} . Such lines were also used to measure the instrumental profile width, which is slightly higher ($\sim 40 \text{ km s}^{-1}$) than the nominal one. The line velocity spread (Δv) was measured by deconvolving the measured instrumental profile with the observed line profile. The peak radial velocity (v_{peak}) was calculated with respect to the ambient molecular cloud, for which a velocity of 4.5 km s^{-1} in the local standard of rest (LSR) has been adopted (Liseau et al. 1992). We report in Fig. 3 the line profiles of the inner knots D1 and F0, while in Table 3 the velocity parameters of all the encompassed knots are given.

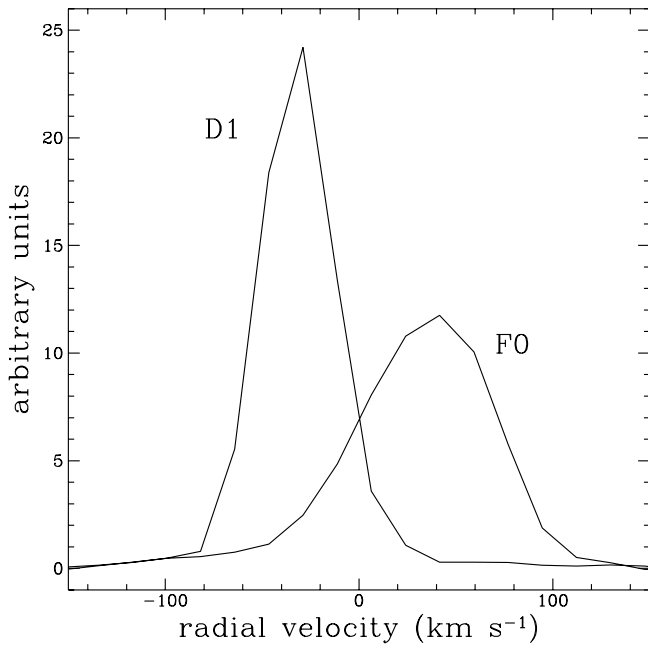


Fig. 3. Medium-resolution profile of the H_2 2.1218 μm line of the knots D1 and F0, which are symmetrically located with respect to the candidate exciting source. The velocity is referred to the ambient cloud velocity.

Table 3. Medium-resolution spectroscopy parameters.

Knot	v_{peak}^a (km s^{-1})	$FWHM$	Knot	v_{peak}^a (km s^{-1})	$FWHM$
A_{1a} †	-8	28	D_2	-28	31
A_{1b} †	-11	33	F_0	35	72
A_2	-8	24	F_1	34	54
A_3	-6	22	G_1	22	38
B_2	-16	20	G_2	13	30
C_1	-23	26	G_3	11	26
C_2	-22	30	H_1	10	19
C_3	-18	27	I	3	19
C_4	-15	25	E_1	-6	41
C_5	-22	29	E_2	-9	43
D_1	-32	27	E_3	-11	55

Note: ^a Computed with respect to the ambient cloud velocity.

† Knot A_1 is further resolved in A_{1a} and A_{1b} .

2.2. Observations in the mm range

2.2.1. Imaging

Observations of the continuum emission at 1.2 mm were carried out on May 23, 2003 using the 37-channel bolometer array SIMBA (Nyman et al. 2001) at the Swedish-ESO Submillimetre Telescope (SEST, La Silla, Chile). At this wavelength, the beam HPBW is $24''$. A region of $18' \times 14'$ (azimuth \times elevation) centred on IRAS08448-4343 was mapped four times in the fast scanning mode, with a scanning speed of $80'' \text{ s}^{-1}$. These observations are part of a program aimed to map a much larger area of the VMR. The pointing was always better than $5''$. This also has been assumed as an estimate of

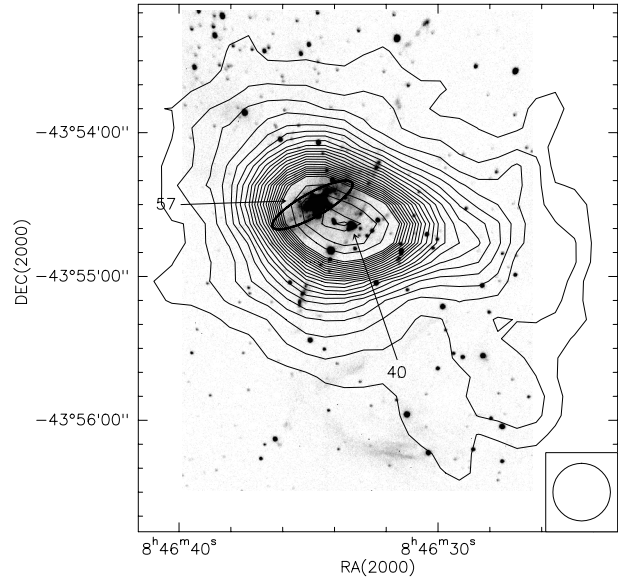


Fig. 4. The 1.2 mm continuum emission map overlaid with the SofI/NTT image (by L02) through the H_2 narrowband filter (centred at 2.12 μm). The contour levels range from 45 to 990 mJy/beam in steps of 45 mJy/beam ($\sim 3\sigma$) and from 1000 to 1670 mJy/beam in steps of 200 mJy/beam. The coordinates of the mm peak are: $\alpha_{(2000)} = 08^{\text{h}}46^{\text{m}}33.6^{\text{s}}$, $\delta_{(2000)} = -43^{\circ}54'38''$. The beam size is shown in the bottom right corner. The IRAS uncertainty ellipse (95% of confidence) is also drawn and the NIR sources #40 and #57 are indicated.

the astrometric accuracy; indeed, in the fast scanning mode the array moves along the map during the measurement and thus a large spatial oversampling is achieved. The zenith atmospheric opacity was measured every ~ 2 h, as well, through skydips and varied in the range of 0.260–0.320.

All data were reduced with MOPSI¹ according to the SIMBA observer's handbook (2003). The steps are summarized in Chini et al. (2003). All 4 maps were coadded and the residual noise in the final image is ~ 15 mJy/beam. The calibration was performed by observing Uranus and Jupiter. The conversion factor from counts to mJy/beam remained quite stable (within $\sim 10\%$) and we adopted the standard value of 65 mJy/beam counts⁻¹, which we found to always approximate the actual value better than 10%. In Fig. 4 we show the map of the 1.2 mm continuum emission overlaid with the $5' \times 5'$ SofI image (taken from L02) through the H_2 narrowband filter. The structure appears to peak towards the source #40 rather than #57. Nevertheless, the emission is quite intense towards #57, as well. The IRAS uncertainty ellipse does not coincide with the mm peak (see again Fig. 4); this means that in the mid- and far-infrared, most of the emission comes from a region around #57, whereas towards #40 it is much fainter at those wavelengths. This suggests that the eastern part of the 1.2 mm emission arises in a more evolved region with warmer dust, whereas the western part, peaking at #40, traces a less evolved region with colder dust.

Photometry and analysis were carried out using MOPSI and GRAPHIC. A resolved dust structure encloses most of the

¹ MOPSI is a software package for infrared, millimetre and radio data reduction developed and regularly upgraded by R. Zylka.

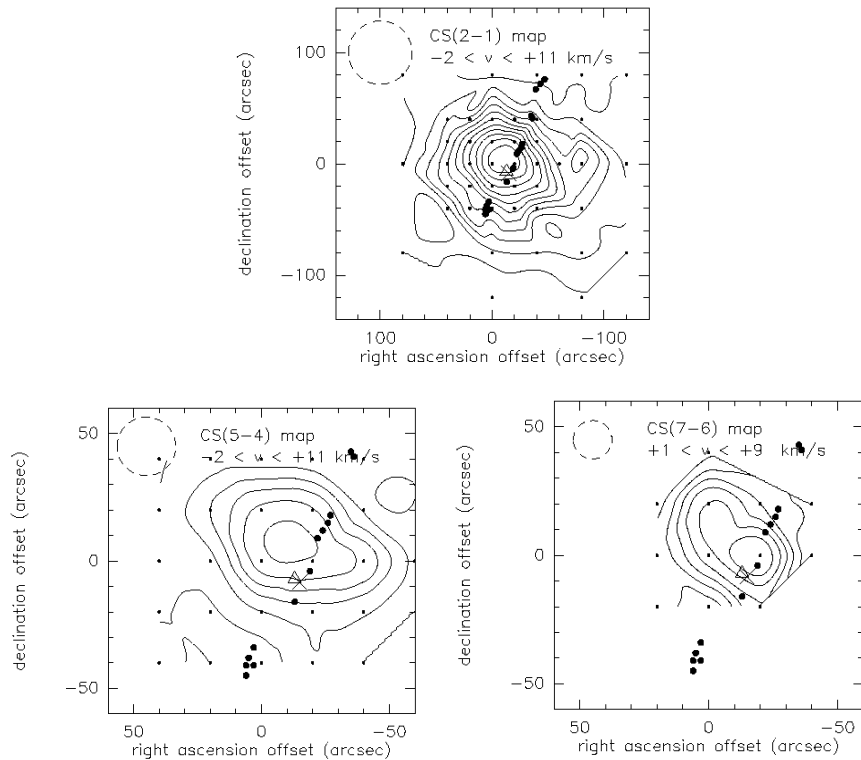


Fig. 5. The distribution of $\int(T_{\text{MB}}dv)$ for CS(2–1) (top), CS(5–4) (bottom left) and CS(7–6) (bottom right). Lowest contour level and contour step are : 1 and 2 K km s⁻¹ for CS(2–1) and CS(5–4); 0.5 and 0.5 K km s⁻¹ for CS(7–6). The grid positions (arcsec) are offsets from the IRAS source. The position of complex #40 and of the dust peak are marked with a cross and a triangle, respectively. The beam size is shown in the top left corner. Dots indicate the knots of the H₂ main jet.

cluster, exhibiting a total flux of 8784 ± 265 mJy. Since the radio-continuum emission at 4.85 GHz lies below the detection limit (48 mJy) of the Parkes-MIT-NRAO survey (Griffith & Wright 1993), most of the 1.2 mm emission is due to thermal radiation from cold dust. Selecting an aperture with a diameter equal to the beam HPBW and centred on the position of the IRAS point source, we measured a flux of 1139 mJy, which is consistent with the single pointing value quoted in M99 for the same position (1111 mJy). The same calculation centred on source #40 gives a flux of 1321 mJy.

2.2.2. Spectroscopy

Observations of the CS lines: $J = 2-1$ at 97.98 GHz, $J = 5-4$ at 244.94 GHz, $J = 7-6$ at 342.88 GHz and $\text{C}^{34}\text{S } J = 2-1$ at 96.41 GHz, were conducted at the SEST in June 1994. We used the heterodyne receivers IRAM115, IRAM230 and NDW350, whose characteristics are given in Table 1, with the high-resolution acousto-optical spectrometer as a backend. Raster maps in CS and $\text{C}^{34}\text{S } J = 2-1$ covering a region of about $160'' \times 160''$ around IRAS08448-4343 source were made with a spacing of $20''$ near this source and $40''$ in the outer parts of the map. Maps in CS $J = 5-4$ and $J = 7-6$ cover smaller regions of $80'' \times 80''$ and $60'' \times 40''$, respectively, with a spacing of $20''$. For each map we indicate in Table 1 the spatial and spectral resolution (Cols. 5, 7), the number of the pointed

positions (Col. 6) and the total integration time (Col. 8). The observations were carried out in frequency-switch mode to compensate for possible instabilities in the gain of the receivers and to subtract the sky emission. The system temperature during the observations was $T_{\text{sys}} = 404.5$ K for IRAM115, 697.7 K for IRAM230 and 1039 K for NDW350. To convert the antenna temperature (T_{A}) into main beam brightness temperature (T_{MB}), a main beam efficiency η_{MB} equal to 0.70, 0.50 and 0.25 was adopted at the frequencies of the 2–1, 5–4 and 7–6 transitions, respectively. The pointing accuracy was about $3''$. The distribution of the CS line integrated intensities in the considered transitions is given in Fig. 5. The morphology of the CS $J = 2-1$ map is similar to that shown by WB99, showing a peak coincident within 20 arcsec with the position of the IRAS source. The same behaviour is exhibited by the emission in the $J = 5-4$ line; on the contrary, the peak of the $J = 7-6$ map is shifted toward the south-west by ~ 15 arcsec, i.e. closer to the location of complex #40. This effect, which stems both from the increasing spatial resolution at higher frequency measurements and from the better sensitivity of higher- J transitions in tracing higher densities, points to the presence of a peak of the gas density in the neighborhood of source #40. Noticeably, independent evidence of this can be deduced if the visual extinction toward #40 (~ 30 mag, see Sect. 2.1.2) is compared with the determination of 20 mag derivable, through the calibration given by Murakawa et al. (2000), from the $3 \mu\text{m}$ ice feature in the spectrum of source #57 (Dartois et al. 2003).

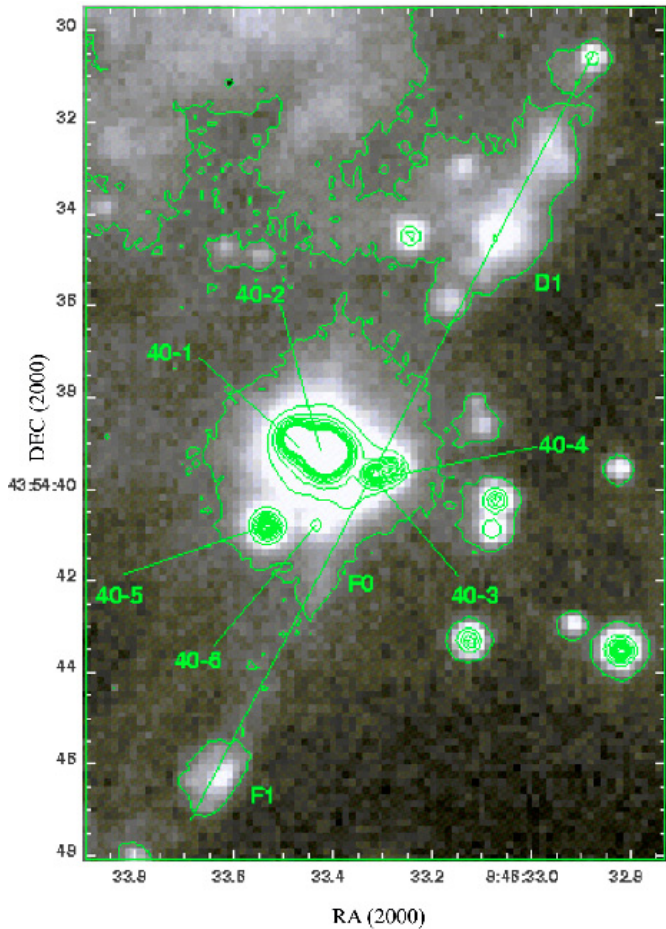


Fig. 6. Countour plot showing the H_2 emission (not continuum-subtracted) around the source #40. Contours are in steps of 9σ from a 3σ level of $9 \times 10^{-17} \text{ erg s}^{-1} \text{ cm}^{-2} \text{ arcsec}^{-1}$. At the ISAAC spatial resolution, #40 is resolved into six $2 \mu\text{m}$ peaks, labelled from 1 to 6. Among them, #40-3 is that better aligned with the inner knots of the main jet (F0, F1 and D1).

3. Analysis and discussion

3.1. Jet morphology and properties

As already discussed by L02, in the continuum-subtracted H_2 image of the IRS17 field (their Fig. 3) several jets can be recognized, the most prominent one being a sub-parsec scale jet composed of the knots from A to K, which is only partially encompassed by the ISAAC field of view (knots from A to I). The higher spatial resolution of the present observations allow us to resolve the source #40, which was proposed as the jet driving source, in at least six $2 \mu\text{m}$ peaks (see Fig. 6, where the contours above the 3σ level are depicted). Such sources are most likely of stellar nature since they do not appear in the H_2 continuum-subtracted image. The photometry of those sources which have been resolved both in the K and H filters is provided in Table 4. Their $(H - K)$ colours range between 1.3 and 1.8 mag, similar to the colour of the #40 complex as a whole (Table 4). However, the spectral classification of these sources cannot be determined from the $(H - K)$ colour alone. Out of the six peaks, that identified as #40-3 appears the best aligned with

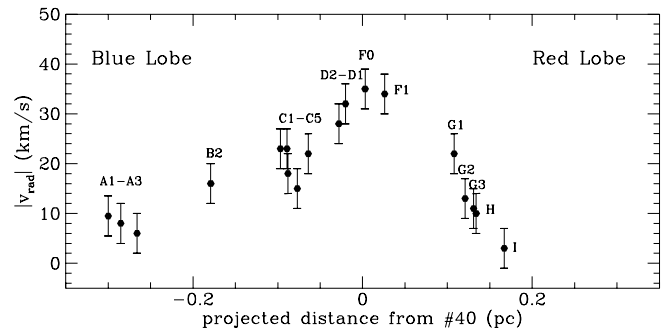


Fig. 7. Radial velocity as a function of the distance from #40.

the closest knots D1, F0 and F1: this makes #40-3 as the most favourable candidate for the jet driving source.

To derive the kinematical properties of the jet, we plot in Fig. 7 the radial velocity component observed in each knot (reported in Table 3) as a function of the distance from the #40 complex. The data points clearly show that the highest radial velocities are related to the jet base, which positionally roughly coincides with the exciting source. The data of Table 3 allow us to firmly identify a redshifted (in the SE direction) and a blueshifted (in the NW direction) lobe of the jet. Such a finding confirms the preliminary interpretation given in L02 relying only on the higher values of the visual extinction ($A_V \sim 20$ mag) found in the correspondence of the SE knots with respect to those of the NW ones ($A_V \sim 10$ mag). In this framework, we interpret the different slope of the velocity in the two lobes (clearly seen in Fig. 7) as due to the higher density of the medium in the red lobe direction, which points towards the inner part of the cloud core: in this case the energy is efficiently dissipated at relatively short distances from the exciting source.

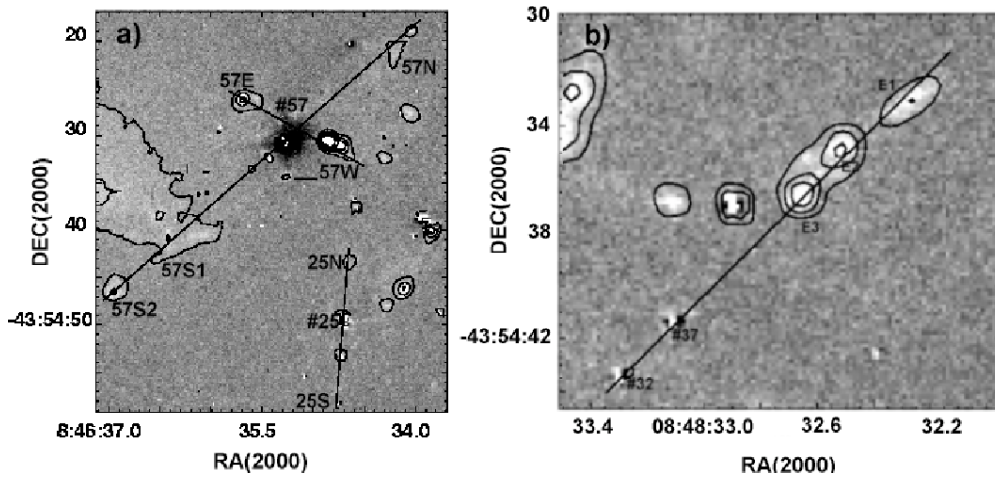
Remarkably, the effect represented in Fig. 7, namely the decreasing of the knot radial velocity component increasing with distance from the exciting source, is apparently in contrast with the behaviour shown by L02 in their Fig. 9, according to which the excitation temperature, and in turn the shock velocity, increases from the base towards the apex of the jet, a trend also confirmed by the results from the low-resolution spectroscopy of the inner knots (Sect. 2.1.2). This contradiction however can be easily reconciled if we interpret the plot in L02 as an effect of the high extinction, which tends to hide the H_2 lines with higher vibrational number ($v > 1$) lying at wavelengths shorter than $1.4 \mu\text{m}$. Such lines are indeed crucial to probe components with a temperature higher than 3000 K (e.g. Giannini et al. 2002). If this is the case, an artificial decrease of the excitation temperature could have been simulated in the more embedded zones (those nearest to the exciting source). Remarkably, the proposed interpretation is supported by the detection (although with a poor signal to noise ratio) of the $[\text{Fe II}] 1.644 \mu\text{m}$ at the jet base (see Table 2), a line commonly excited in dissociative shock environments, where velocities higher than 30 km s^{-1} are typically attained (Hollenbach & McKee 1989).

An opposite interpretation of the observed velocities could be given if we consider that they might refer to the radial component, which can decrease if the jet inclination changes with the distance from the driving source, approaching the sky

Table 4. Infrared photometry of the sources in the IRS17 field which have been recognized as possible exciting sources of the discovered jets.

Source	H (mag)	K (mag)	L (mag)	M (mag)	N ^a (mag)
25	12.00 ± 0.01	10.70 ± 0.00	8.966 ± 0.03	8.46 ± 0.06	5.7 ± 0.3
32	15.40 ± 0.03	14.34 ± 0.03	>13.5	>10.7	–
37	15.89 ± 0.04	13.78 ± 0.01	10.74 ± 0.04	9.73 ± 0.08	>6 ^b
40 ^c	12.40 ± 0.01	10.71 ± 0.00	8.918 ± 0.03	8.64 ± 0.06	6.1 ± 0.4
40-1	13.69 ± 0.02	12.34 ± 0.01	–	–	–
40-2	12.97 ± 0.01	11.12 ± 0.00	–	–	–
40-3	15.32 ± 0.03	13.98 ± 0.01	11.98 ± 0.05	10.9 ± 0.3	–
40-5	15.52 ± 0.03	14.12 ± 0.03	–	–	–
57	13.16 ± 0.01 ^d	9.92 ± 0.00 ^d	5.882 ± 0.03	4.876 ± 0.06	1.64 ± 0.2

Notes:

^a The reported error includes the uncertainty associated with the calibration procedure (see text).^b 3 σ lower limit.^c Photometry integrated over the six peaks which contribute to #40.^d Photometry taken from M99 since this source is saturated in our ISAAC image.**Fig. 8.** **a)** Contours of the H₂ (continuum-subtracted) emission in the neighborhood of source #57. The identified jets are indicated with straight lines. Contours are in steps of 1 σ , from a 2 σ level of 6×10^{-17} erg s⁻¹ cm⁻² arcsec⁻¹. **b)** Contours of the H₂ (continuum-subtracted) emission of the knots E1–E3, from a 4 σ level of 1.2×10^{-16} erg s⁻¹ cm⁻² arcsec⁻¹ and in steps of 2 σ . In both panels knots of shocked gas as well as stars recognized as intrinsically red by M99 are labelled.

plane. Such behaviour could occur if, e.g., the jet morphology we are observing is the projection on the sky plane of a rotating jet which lies on the surface of two paraboloids with #40-3 at their common vertex. In this framework, the highest radial velocities should be measured on the knots closest to the exciting source (namely F and D), while decreasing values should apply to the knots more and more distant from #40-3. Such a view is supported by the fact that the northern lobe of the jet (made up of the knots C, B and A) appears elongated in a direction counterclockwise rotated by roughly 10° with respect to the line defined by the alignment of the inner knots (that depicted in Fig. 6). To have the same trend in the southern lobe, we should assume that knot G does not belong to the main jet because of the misalignment with respect to the individuated direction. In this case, however, we should consider as a fortuitous coincidence the compatibility of the v_{rad} values relative to the knots G1–G3 with those of the nearby knots (see Table 3). This in our opinion makes the former interpretation (i.e. the jet

velocity *decreasing* with the distance from the exciting source) the most reconcilable with the observed data, even if a conclusive statement cannot be firmly pronounced. An answer in a statistical sense can be obtained from the high-resolution spectroscopic observations accumulated in the literature. So far, however, the existence of a definite trend has not been ascertained. A number of objects show increasing values of the radial velocity with distance: HH219 – low velocity component (LVC, Caratti o Garatti et al. 2004), HH111 – LVC (Davis et al. 2001); HH212 (Davis et al. 2000); HH120 (Schwartz & Greene 2003), HH46/47 (Fernandez 2000). Others, such as HH7-11 (Davis et al. 2000) and the HH111-high velocity component (HVC, Davis et al. 2001) show the opposite trend, while some show no clearly definable behaviour: e.g. HH26 and HH33/40 (Davis et al. 2000). Accurate determinations of the velocity tangential components will be of great help to resolve this issue.

In Fig. 8 we show the enlargements of Fig. 1 highlighting other manifestations of mass flows; in panel a): i) the knots

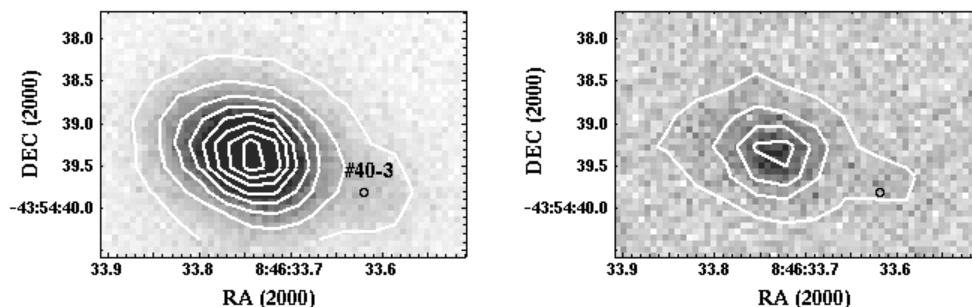


Fig. 9. Enlargements of the L and M images around source #40. In the L image contours are in steps of 3σ from a 3σ level of $\sim 4 \times 10^{-13} \text{ erg s}^{-1} \text{ cm}^{-2} \text{ arcsec}^{-2}$ while in the M image contours are in steps of 2σ from a 2σ level of $\sim 7 \times 10^{-13} \text{ erg s}^{-1} \text{ cm}^{-2} \text{ arcsec}^{-2}$. The position of #40-3 is indicated by a small circle in both panels.

57N and 57S, apparently emanating from the source #57 are detected only at the 2σ level; ii) the knots 57E and 57W are symmetrically located with respect to a central, unidentified source, which should lie a few tenths of an arcsec to the NW of #57; the presence of such an object is revealed by the elongation to the NW of the intensity contours in all the broadband images in the thermal IR, even if our spatial resolution is too poor to disentangle a faint object from the bright nebosity around the IRAS source; iii) two faint knots, labelled as 25N and 25S, are detected at the 2σ level and are displaced in the north-south direction with respect to two stars. One of these is the #25, a source which has red intrinsic colours typical of young protostars (M99). A further, blue-shifted (see Table 3) jet is composed of the knots E1, E2 and E3, which are well aligned with #32 and #37, suggesting one of them as the possible exciting source (Fig. 8, panel b). The intrinsic faintness of this jet (L02) provides a plausible reason for the lack of a red-shifted counter jet, that moreover should be located in a region where the measured visual extinction is about 30 mag (see Sect. 2.1.2). Finally, other faint condensations, shown by dashes in Fig. 1, are recognizable throughout the field and are difficult to be morphologically associated with any of the jets described above.

In conclusion, at least five different jets exist in the IRS17 region, that associated with #40 being the most prominent one. Such a complex morphology is indeed not uncommon in young stellar clusters, as IRS17 is (Massi et al. 2000), and maybe it is at the origin of a certain degree of confusion in the CO map presented by WB99 (their Fig. 4), where the lack of a well-defined CO outflow is evident. The presented case is therefore in support of the fact that molecular outflows from intermediate- and high-mass stars in general appear poorly collimated because of the superposition of outflows coming from different sources (e.g. Beuther et al. 2004; Nanda Kumar et al. 2002) and is not due to growth processes (e.g. coalescence), different from those occurring in low-mass star-forming regions (e.g. Stahler et al. 2000; Bally 2002).

3.2. Exciting sources

All the objects candidate to be the driving sources of the discovered jets (Sect. 3.1) have been found by M99 to exhibit

intrinsic red colours in the J , H and K bands. To better understand their nature at longer wavelengths, we have imaged the IRS17 field in the L , M and N bands (Fig. 2). Remarkably, in the M image, only four stars, namely #57, #25, #40 and #37, which are aligned with the jets of the region, are detected above the 3σ limit. Three of them (#57, #25, #40) are also visible in the N filter, while the fourth (#37) is barely detected at about the 2.3σ level. The non-detection of source #32 in all the thermal filters suggests that this object is more evolved with respect to source #37, which is thus favoured as the powering source of the E1–E3 jet. The broadband photometry of the mentioned stars is reported in Table 4. In the H and K bands, the derived magnitudes agree within a few tenths with the values measured by M99. In particular, we refer to that paper for the H , K magnitudes of #57, which is saturated in our ISAAC images.

The case of #40 deserves a more detailed analysis. As traced by the mm-emission, the jet originates in a zone colder and less evolved than that corresponding to the IRAS peak. Here a sub-cluster is present, which has been partially resolved in the K band (Fig. 6): this has allowed us to assign to #40-3 the role of possible driving source of the jet. In this context, it seems worthwhile to evaluate the photometric properties (mid and far IR colours) and the luminosity of the #40 complex, aiming to investigate whether it harbours the IR counterpart of a mm-source powering the jet.

We are able to disentangle the H , K band contributions coming from four out of the six sources in which such a complex is resolved. The same was not possible in the L , M and N filters, since the emission tends to be more diffuse at increasing wavelengths because of diffraction effects. Thus we give the photometry in such bands by considering the #40 complex as a whole. However, in L and M bands, we are able to evaluate the relative contribution of #40-3 to the total emission by performing aperture photometry at the coordinates of this source (see Table 4). Noticeably, the $(L - M)$ colour of #40-3 is 1.0 ± 0.3 , i.e. definitely redder than that (0.28 ± 0.07) of source #40 as a whole. This circumstance favours #40-3 as the youngest member of the complex.

The bolometric luminosity (L_{bol}) of #57 and #40 has been obtained by integrating their flux densities from $1.6 \mu\text{m}$ to 1.2 mm . While in the near IR and in the mm regimes both contributions are separable (see Table 4 and Sect. 2.2.1), some

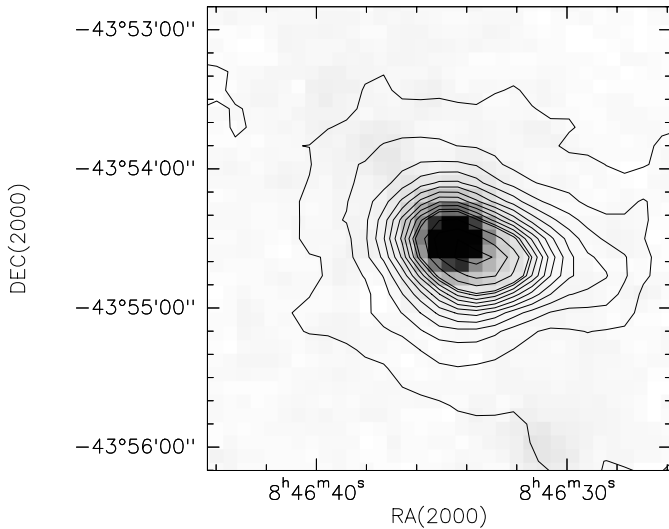


Fig. 10. The 1.2 mm continuum emission map overlaid with the MSX greyscale image in the *E* band ($21.3 \mu\text{m}$). The contour levels range from 45 to 990 mJy/beam in steps of 90 mJy/beam and from 1000 to 1600 mJy/beam in steps of 200 mJy/beam.

assumptions are needed to disentangle the IRAS contributions. In particular, the fluxes measured by IRAS at 12 (8.7 Jy), 25 (88.05 Jy), 60 (326.60 Jy) and 100 (1005.0 Jy) μm have been attributed in the L_{bol} calculation to source #57, although #40 is encompassed by the IRAS beam at these wavelengths. Such an assumption appears reasonable at 12 and 25 μm , as demonstrated by both our 10 μm photometry, according to which #40 is about 4 mag fainter than #57, and by the MSX image at 21.3 μm (resolution $\sim 17''$): this latter, which is shown in Fig. 10 overlaid with the 1.2 mm continuum map, clearly shows the mid-infrared source lying eastward #40 and almost centred on #57. Moreover, the IRAS fluxes are flagged as due to a point-like source at 12 and 25 μm ; on the contrary a certain degree of extendedness is signaled at 60 and 100 μm . Such a circumstance, along with the strong peak detected at 1.2 mm, suggests that the emission from the #40 complex becomes more and more relevant at far-infrared and millimetre wavelengths. Aiming to determine a plausible range for the #40 luminosity, in Fig. 11 we show the spectral energy distribution (SED) of #40 obtained by arbitrarily assuming at 60 and 100 μm one hundredth (short-dashed line) and half (long-dashed line) of the IRAS fluxes: this corresponds to $L_{\text{bol}} = 11$ and $245 L_{\odot}$, respectively. We remark that, although both these values, due to the source multiplicity, provide an upper limit to the bolometric luminosity of #40-3, this object is, as suggested by its $L-M$ colour, probably the one in the #40 complex which dominates at the longest wavelengths, i.e. where a significant contribution of L_{bol} is given.

Summarizing, the accumulated observational material favours #40-3 as the driving source of the main jet and as the NIR counterpart of the 1.2 mm source. This newly identified object is a low-mass YSO which could be in an evolutionary stage known as class I, during which the observed SED shows an almost flat behaviour over a wide range of

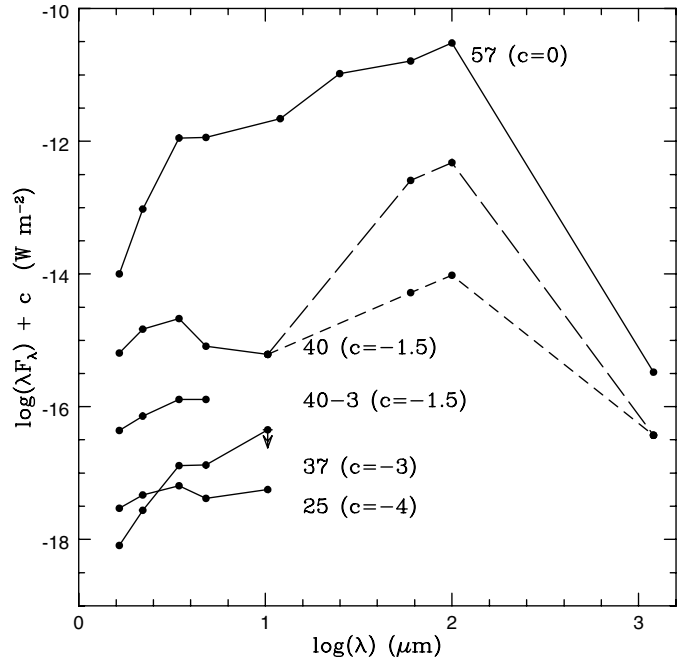


Fig. 11. Spectral energy distribution of the sources identified as the possible drivers of the H_2 jets in the field. The #40 SED is represented by the long-dashed and short-dashed lines if half and one hundredth of the 60 and 100 μm IRAS fluxes is attributed to this source, respectively. The L and M points of #40-3 correspond to the magnitudes computed with aperture photometry at the source coordinates. The downward arrow represents the 3σ lower limit of the magnitude in *N* band of #37.

Table 5. Comparison between the bolometric luminosity of the candidate driving sources and the H_2 luminosity of the excited jets.

Source	L_{bol} (L_{\odot})	$L_{\text{H}_2}^a$ (L_{\odot})	$L_{\text{H}_2}/L_{\text{bol}}$
25	$>2.6^b$	2.0×10^{-3}	$<8 \times 10^{-4}$
37	$>1.3^b$	1.6×10^{-2}	$<1.2 \times 10^{-2}$
40	11–245	3.1×10^{-1}	2.8×10^{-2} – 1.3×10^{-3}
57	715 ^c	4.5×10^{-2}	6.3×10^{-5}

Notes: ^a Computed by assuming the following A_V values: 10 mag for #25 and 37 jets, 18 mag for #57 jet (L02). For the main jet we adopted, for each knot, the extinction value derived by the low-resolution spectroscopy.

^b Derived by assuming blackbody extrapolation longward the last photometric point (that in *N* band).

^c Revised with respect to the value given by M99.

wavelengths spanning from the near-infrared to the mm range (e.g. Whitney et al. 2003).

In addition to #40 and #57, we give in Table 5 the bolometric luminosities derived also for #25 and #37. These have been calculated by adopting the correction given by Cohen (1973), which extrapolates the SED with a blackbody function peaking at the last photometric point (that in *N* band in our case). From the shape of the SEDs, we cannot exclude that the peak is indeed at wavelengths longer than 10 μm : in this sense the values reported in Table 5 have to be considered as lower limits to L_{bol} . However, the absence of millimetre peaks

corresponding to the #25 and #37 locations, suggests that the bolometric luminosities of these two sources are significantly lower than those of #40 and #57.

3.3. Energy budget

The ratio between the luminosity irradiated away through the H₂ line emission (L_{H_2}) and the bolometric luminosity (L_{bol}) is an empirical indicator of the evolutionary stage of the sources driving outflowing matter. Such a ratio allows us to roughly evaluate the efficiency in transferring energy from the central source into the jet and, as such, it is expected to decrease during the evolution (e.g. Stanke 2000). This parameter is listed in Table 5 for all the sources in this field which are candidates to drive a jet and #40 shows the highest ratio, with the possible exception of #37. Concerning the main jet, the 1–0 S(1) flux has been evaluated by adding the 2.122 μm fluxes of the knots reported by L02 and those in Table 2, once corrected for the indicated visual extinction. For the other jets the 2.122 μm intrinsic flux has been derived by the photometry of the H₂ continuum-subtracted image, by adopting $A_V = 10$ mag for #25 and #37 jets and 18 mag for #57 jet (L02). By considering that for a thermalized gas at ~ 2000 K the flux of the 1–0 S(1) line is about a tenth of the total H₂ luminosity and assuming a distance of 700 pc (Liseau et al. 1992), we obtain for the main jet $L_{\text{H}_2} = 0.31 L_{\odot}$, which yields a ratio $L_{\text{H}_2}/L_{\text{bol}}$ between 2.8×10^{-2} – 1.3×10^{-3} . Note that such a ratio shows only a marginal decrease (by less than 10%) if the knots of group G are not considered to belong to the main jet (Sect. 3.1). Similar values are more typical of poorly evolved sources, i.e. the class 0 protostars (Bally et al. 1993; Davis & Eisloffel 1995; Lefloch et al. 1996; Nisini et al. 2000). The spectral energy distribution of such sources resembles that of a single temperature grey-body at $T \sim 15$ – 30 K (André et al. 1993): this implies that the emission in the near-infrared is negligible with respect to that at longer wavelengths. Reasonably, the high value of the $L_{\text{H}_2}/L_{\text{bol}}$ ratio we found for #40, combined with the observed SED, suggests that this object is a very young class I protostar, perhaps intermediate between 0 and I. Alternatively, but contrasting with several of the derived morphological and physical properties, the peak discovered at 1.2 mm could effectively reveal the presence of a genuine class 0 protostar, but, in such case, the alignment of the jet with one of the reddest sources in the field (i.e. #40-3) should be considered as fortuitous. We note how a substantially increased spatial resolution in the far-infrared and mm range (such as that to be provided by the Spitzer and Herschel space telescopes and by the Atacama Large Millimetre Array), will be crucial to solve this and similar questions.

3.4. Large scale properties

3.4.1. Gas parameters

To derive the physical parameters of the molecular gas, we interpret the CS line intensities in the framework of the large velocity gradient (LVG) approximation, which we retain as valid

Table 6. Output of the LVG model for the CS lines.

$(\Delta\alpha, \Delta\delta)$ (" , ")	τ_{CS}	$N(\text{CS})$ (cm^{-2})	n_{H_2} (cm^{-3})
(0, 40)	2.0	3.1×10^{14}	1.6×10^5
(−40, 20)	3.6	6.3×10^{14}	1.6×10^5
(−20, 20)	2.4	1.2×10^{15}	4.0×10^5
(0, 20)	2.4	1.3×10^{15}	5.0×10^5
(20, 20)	2.8	6.3×10^{14}	2.0×10^5
(40, 0)	1.5	1.6×10^{14}	1.0×10^5
(20, 0)	2.2	6.3×10^{14}	2.5×10^5
(0, 0)	3.0	2.5×10^{15}	6.3×10^5
(−20, 0)	3.0	2.5×10^{15}	1.0×10^6
(−40, 0)	2.9	6.3×10^{14}	2.5×10^5
(−60, 0)	4.2	6.3×10^{14}	1.6×10^5
(0, −20)	2.8	6.3×10^{14}	2.0×10^5
(−20, −20)	3.1	1.3×10^{15}	4.0×10^5
$X(\text{CS})^a$		5.6×10^{-9}	
M_{CS}^a		$214 M_{\odot}$	

Note: ^a Computed over a spherical area with a diameter of 0.25 pc.

since the observed lines are broader ($\Delta v \sim 10 \text{ km s}^{-1}$) than expected if due to the thermal motion alone. In LVG conditions the line intensities, in addition to the optical depth, depend on temperature (T_{kin}) and density (n_{H_2}) of the colliding gas and on the ratio between the CS column density ($N(\text{CS})$) and the velocity spread (Δv). The adopted model solves the equations of the statistical equilibrium for the first 13 levels of CS, by assuming the H₂ collisional coefficients given by Green & Chapman (1978) and the spontaneous emission rates by Chandra & Sharma (2001). To minimize the number of free parameters, we fixed the optical depth of the $J = 2-1$ line from the ratio $\text{CS}(2-1)/\text{C}^{34}\text{S}(2-1)$. In LTE excitation conditions, and assuming the $\text{C}^{34}\text{S}(2-1)$ transition to be optically thin, the same excitation temperature (T_{ex}) for both the lines and $\text{CS}/\text{C}^{34}\text{S} \approx 22$ (Wilson & Rood 1994), the optical depth (τ_{CS}) is derivable from the equation:

$$R \approx (1 - e^{-\tau_{\text{CS}}}) \cdot 22 / \tau_{\text{CS}} \quad (1)$$

where R is the $\text{CS}(2-1)/\text{C}^{34}\text{S}(2-1)$ line ratio.

By integrating under the line profile with a Gaussian fit, we have derived the optical depth, which ranges between 1.5 and 4 over the region covered by the CS map (Table 6). Together with this, we have independently estimated the kinetic temperature of the gas from a large scale CO(1–0) map recently obtained by Elia et al. (in preparation). By considering the points of this map in the neighbourhood of the IRAS source, an average value of $T_{\text{kin}} \approx 23$ K has been estimated, under LTE excitation conditions. Having also fixed Δv from the Gaussian fit of the line profiles, we have applied the LVG model in the positions where, in addition to an estimate of τ_{CS} , at least two CS lines with a signal-to-noise ratio greater than three have been observed.

The output parameters of the model, namely $N(\text{CS})$ and n_{H_2} , are reported in Table 6 and indicated in Fig. 12 superimposed on the $J = 7-6$ line map. Here it can be seen that, in agreement with the elongation westward evidenced by the

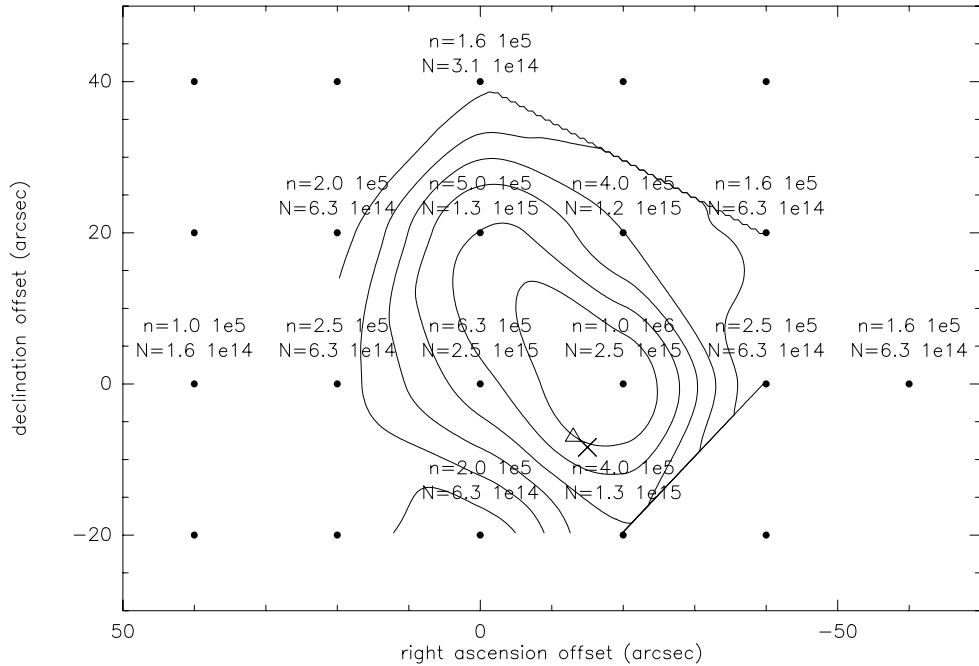


Fig. 12. Output of the LVG model for the CS emission. The yielded values of $N(\text{CS})$ (cm^{-2}) and n_{H_2} (cm^{-3}) are superimposed on the CS $J = 7-6$ map. Source #57 is in (0, 0). Source #40 and the dust peak are indicated with a cross and a triangle, respectively.

$J = 7-6$ morphology, both the volume and column densities peak in the position ($-20''$, $0''$), which is shifted by about 7 arcsec both in right ascension and declination with respect to the dust peak (and source #40). Since the three transitions of CS have been obtained at different resolution, due to the different beam-dilution degree, the yielded densities are likely to be overestimated. Anyway we expect the effect to be small and not to affect the conclusions on the location of the density peak.

Averaging the values of $N(\text{CS})$ and n_{H_2} we estimate the core parameters listed at the bottom of Table 6. We define the core effective diameter ($\sim 74''$, i.e. 0.25 pc) as the geometric average of the major and minor axis of the area in the CS(2-1) map at half-intensity level. By assuming a spherical geometry, a gas mass of $214 M_{\odot}$ is derived, which is in good agreement with the determination of $260 M_{\odot}$ obtained from C^{18}O in LTE approximation (WB99). From the total mass and $N(\text{CS})$, an average CS abundance, $X(\text{CS})$, of 5.6×10^{-9} is derived. This value is within the very wide range ($\sim 5 \times 10^{-10}$ – 2×10^{-7}) typically measured in the outflows of protostars and in protostellar cores (e.g. Bottinelli & Williams 2004; Jørgensen et al. 2004; Shirley Y.L. et al. 2003). We note, however, that $X(\text{CS})$ is enhanced by about 50% toward the peak of the CS(7-6) emission, as expected in cores in the very first stages of evolution (Bergin & Langer 1997).

3.4.2. Dust parameters

In Fig. 4 the 1.2 mm emission appears to arise from a compact component superimposed on a more diffuse one. We tried to separate the compact and the diffuse components by fitting a 2D Gaussian and subtracting it from the map. We made use of the task GFIT in MOPSI, centring the fit at the location of the mm peak. This revealed two compact components: a first

one, named mmA, which is separated by few arcsec both in right ascension and declination from the peak of the integrated intensity; and a second, fainter component, (mmB), whose total flux and size were again derived by fitting a 2D Gaussian to the subtracted map. Coordinates and sizes of mmA and mmB are listed in Table 7. Note that mmB lies towards a region with a low density of stars, probably tracing a still unevolved site of star formation within the cluster.

Mass, volume-averaged hydrogen density and source-averaged hydrogen column density were derived by using the relations in Henning et al. (1998) for 1.3 mm continuum fluxes. The most critical parameters are the dust mass opacity and the temperature. We assumed a dust mass opacity (at 1.3 mm) of $k_{1.3} \sim 0.5 \text{ cm}^{-2} \text{ g}^{-1}$, the same as used for dense pre-stellar clumps and cores in ρ Ophiuchi (Motte et al. 1998) and Serpens (Testi & Sargent 1998). However, note that $k_{1.3}$ could be as high as $1 \text{ cm}^{-2} \text{ g}^{-1}$ in very dense regions (thus decreasing both the mass and the density by a factor 2; Ossenkopf & Henning 1994), or as low as the interstellar value of $0.26 \text{ cm}^{-2} \text{ g}^{-1}$ (thus doubling the mass and density, as could be the case in low density regions such as the diffuse component; Hildebrand 1983). For the dust temperature, we assumed 23 K, derived from the CO(1-0) emission, for consistency with the analysis of mm line emission. This could underestimate the true temperature around #57, and might be too large in inner, less evolved regions such as mmB. It is easy to check that decreasing it to 15 K would yield an increase of a factor of 1.8 in the derived masses and densities. On the other hand, a dust temperature as high as 60 K would result in a decrease of masses and densities by a factor 3. By propagating the error on the distance (200 pc; see Liseau et al. 1992) we obtain a further uncertainty of 29% on the volume density and 57% on the gas mass. We have also assumed a solar metallicity. The results are given in

Table 7. Physical parameters derived from the 1.2 mm continuum emission.

Source	Centre		Size ^a (HPBW) (pc × pc)	Total flux (mJy)	Gas mass (M _⊙)	Gas density (cm ⁻³)	Gas column (cm ⁻²)	A _V (mag)
	α(2000.0) (h m s)	δ(2000.0) (° ′ ″)						
mmA	08 46 33.8	-43 54 36	0.16 × 0.09	5284 ± 137	110	1.7 × 10 ⁶	6.4 × 10 ²³	674
mmB	08 46 28.6	-43 54 42	0.14 × 0.08	529 ± 97	11	2.5 × 10 ⁵	8.1 × 10 ²²	85
diffuse			0.59	2810 ± 334	58	7.2 × 10 ³	1.3 × 10 ²²	14

Note: ^a Deconvolved from beam size (24").

Table 7. The volume-averaged densities are in agreement with those derived from CS (see Table 6) and with the determination (averaged in a 44" beam) given in Faundez et al. (2004). The total inferred mass ($\sim 179 M_{\odot}$) is consistent with the value from line observations, i.e., from CS and C¹⁸O. This indicates that, within the uncertainties, the dust-to-gas ratio in the region appears to be consistent with the standard one.

The total extinction obtained from the source-averaged column density of mmA is much larger than that obtained from the NIR colours of the stars towards IRS 17 ($A_V \leq 40$ mag; see Massi et al. 2000). This could indicate that the NIR observations probe only a small fraction of the cloud core volume.

4. Summary

The paper presents a multiwavelength study, from near-infrared to the radio, of the star-forming region IRS17 in the Vela Molecular Ridge. Our observations allowed us to characterize the star formation process occurring in the region at very different spatial scales and led to the following conclusions:

- The emission from dust peaks near the centre of an infrared cluster. The coldest dust component is located westward with respect to the IRAS source, a result which could be common in the young clusters of intermediate- and high-mass star-forming regions and which thus imposes some caution in the association of mm peaks with IRAS sources.
- The dust peak lies in the proximity of a small sub-cluster (#40 in our internal classification) which should include the source driving the sub-parsec scale jet.
- The gas emission has been traced by means of selected CS transitions. The peaks of the lower- J transitions coincide with the IRAS source, while the $J = 7-6$ emission peaks closer to #40. This effect points to the presence of a peak of the gas density in the neighborhood of #40.
- The ISAAC spatial resolution has allowed us to resolve sub-cluster #40 into at least six peaks. The reddest of them, which we label as #40-3, is well aligned with the inner knots of the jet. We thus identify #40-3 as the driving source of the jet. Its spectral energy distribution resembles that of a class I protostar; the very high efficiency in transferring energy into the jet suggests however that this source is one of the youngest members of this class. The presence in the #40 complex of more embedded, undetected sources, is in principle conceivable, even if the presented observational evidence does not necessarily require this.

- Through high-resolution spectroscopy, the blue- and redshifted lobes of the sub-parsec scale jet have been identified. The measured radial velocities progressively decrease (in modulus) going from the jet base to the apex; this could be due to a loss of kinetic energy because of the interaction of the jet with the ambient medium. We cannot however discard the hypothesis that the observed trend reflects the effect of a favourable inclination of the jet to the sky plane.
- Together with the jet driven by #40-3, many other manifestations of mass flows are recognizable throughout the IRS17 field. Three jets, in particular, can be associated with three objects (namely #25, #37 and #57), showing near-infrared colours typical of young protostars. These, together with #40, are the only sources detected up to the N band.
- The jet multiplicity is likely at the origin of a lack of a defined CO outflow in the region. The presented case is thus in support of the theories which attribute the poor collimation of the outflows in intermediate- and high-mass star-forming region, to geometrical rather than to physical effects.
- The physical parameters of the cloud core have been independently derived from both gas and dust emission. CS columns of 1.6×10^{14} – 2.5×10^{15} cm⁻² and hydrogen densities of 10^5 – 10^6 cm⁻³ have been derived from the LVG analysis of the CS lines. $X(\text{CS})$ is on average 5.6×10^{-9} , with an enhancement of about 50% toward the millimetre peak. The gas mass in the cloud core is $210 M_{\odot}$, a value consistent with the determination from the dust emission ($179 M_{\odot}$). This indicates that the dust-to-gas ratio is quite standard in the region.

The source multiplicity of the region, which is typical of intermediate- and high-mass star-forming regions, has prevented us to clearly disentangling the contribution of the sources in the cluster at the longest wavelengths. For this reason, the presented case is a good target for the forthcoming facilities observing in the far-infrared and mm wavelength range.

Acknowledgements. This research made use of data products from the Midcourse Space Experiment (MSX). Processing of the data was funded by the Ballistic Missile Defense Organization with additional support from NASA Office of Space Science.

References

- André, P., Ward-Thompson, D., & Barsony, M. 1993, ApJ, 406, 122
 Bally, J., Devine, D., Hereld, M., & Rausher, B. J. 1993, ApJ, 406, 122

- Bally, J. 2002, in *Hot Star Workshop III: The Earliest Stages of Massive Star Birth*, ed. P. A. Crowther (San Francisco: ASP), ASP Conf. Ser., 267, 219
- Bergin, E. A., & Langer, W. D. 1997, *ApJ*, 486, 316
- Beuther, H., Schilke, P., & Gueth, F. 2004, *ApJ*, 608, 330
- Bottinelli, S., & Williams, J. P. 2004, *A&A*, 421, 1113
- Caratti o Garatti, A., Giannini, T., Lorenzetti, D., et al. 2004, *A&A*, 422, 141
- Chandra, S., & Sharma, A. K. 2001, *A&A*, 376, 356
- Chini, R., Kämpgen, K., Reipurth, B., et al. 2003, *A&A*, 409, 235
- Cohen, M. 1971, *MNRAS*, 164, 395
- Cuby, J. C., Lidman, C., Johnson, R., Jaunsen, A., Moutou, C. 2004, *ISAAC User Manual*
- Dartois, E., Thi, W.-F., Geballe, T. R., et al. 2003, *A&A*, 399, 1009
- Davis, C. J., & Eisloffel, J. 1995, *A&A*, 300, 851
- Davis, C. J., Berndsen, A., Smith, M. D., Chrysostomou, A., & Hobson, J. 2000, *MNRAS*, 314, 229
- Davis, C. J., Hodapp, K. W., & Desroches, L. 2001, *A&A*, 377, 285
- Doublier, V., Billeres, M., Lo Curto, G., et al. 2003, *TIMM12 User Manual*
- Faundez, S., Bronfman, L., Garay, G., et al. 2004, *A&A*, 426, 97
- Fernandez, A. J. L. 2000, *MNRAS*, 315, 657
- Giannini, T., Nisini, B., Caratti o Garatti, A., & Lorenzetti, D. 2002, *ApJ*, 570, L33
- Green, S., & Chapman, S. 1978, *ApJS*, 36, 483
- Griffith, M. R., & Wright, A. E. 1994, *AJ*, 105, 1666
- Henning, Th., Burkert, A., Launhardt, R., Leinert, Ch., & Stecklum, B. 1998, *A&A*, 336, 565
- Hildebrand, R. H. 1983, *QJRAS*, 24, 267
- Hollenbach, D., & McKee, C. F. 1989, *ApJ*, 342, 306
- Jørgensen, J. K., Hogerheijde, M. R., Blake, G. A., et al. 2004, *A&A*, 416, 603
- Lefloch, B., Eisloffel, J., & Lazareff, B. 1996, *A&A*, 313, L17
- Lidman, C., Cuby, J.-C., Vanzi, L., et al. 2003, *SofI User Manual*
- Liseau, R., Lorenzetti, D., Nisini, B., Spinoglio, L., & Moneti, A. 1992, *A&A*, 265, 577
- Lorenzetti, D., Spinoglio, L., & Liseau, R. 1993, *A&A*, 275, 489
- Lorenzetti, D., Giannini, T., Vitali, F., Massi, F., & Nisini, B. 2002, *ApJ*, 564, 839 (L02)
- Massi, F., Giannini, T., Lorenzetti, D., et al. 1999, *A&AS*, 136, 471 (M99)
- Massi, F., Lorenzetti, D., Giannini, T., & Vitali, F. 2000, *A&A*, 353, 598
- Massi, F., Lorenzetti, D., & Giannini, T. 2003, *A&A*, 399, 147
- Motte, F., André, P., & Neri, R. 1998, *A&A*, 336, 150
- Moorwood, A., Finger, G., Bierechel, P., et al. 1992, *ESO Messenger*, 69, 61
- Murakawa, K., Tamura, M., & Nagata, T. 2000, *ApJS*, 128, 603
- Murphy, D. C., & May, J. 1991, *A&A*, 247, 202
- Nanda Kumar, M. S., Bachiller, R., & Davis, C. J. 2002, *ApJ*, 576, 313
- Nisini, B., Benedettini, M., Giannini, T., et al. 2000, *A&A*, 360, 297
- Nyman, L.-Å., Lerner, M., Nielbock, M., et al. 2001, *ESO Messenger*, 106, 40
- Ossenkopf, V., & Henning, Th. 1994, *A&A*, 291, 943
- Rousselot, P., Lidman, C., Cuby, J.-G., Moreels, G., & Monnet, G. 2000, *A&A*, 354, 1134
- Schwartz, R. D., & Greene, T. P. 2003, *AJ*, 126, 339
- Shirley, Y. L., Evans, N.J.II, Young, K. E., Knez, C., & Jaffe, D. T. 2003, *ApJS*, 149, 375
- Stahler, S. W., Palla, F., & Ho, P. T. P. 2000, in *Protostars and Planets IV*, ed. V. Mannings, A. P. Boss, & S. S. Russell (Tucson: Univ. Arizona Press), 327
- Stanke, T. 2000, Ph.D. Thesis
- Testi, L., & Sargent, A. I. 1998, *ApJ*, 508L, 91
- Wilson, T. L., & Rood, R. 1994, *ARA&A*, 32, 191
- Whitney, B., Wood, K., Bjorkman, J. E., & Wolff, M. J. 2003, *ApJ*, 591, 1049
- Wouterloot, J. G. A., & Brand, J. 1999, *A&AS*, 140, 177 (WB)